



# Settling dynamics of two identical vertically aligned spheres in a thixotropic fluid

Katherine Moseley\*, Michael Fairweather, David Harbottle\*

School of Chemical and Process Engineering, University of Leeds, Leeds, LS2 9JT, United Kingdom

## ARTICLE INFO

### Keywords:

Thixotropy  
Shear thinning  
Particle  
Sedimentation  
Particle image velocimetry

## ABSTRACT

Despite the great relevance of particle dynamics in non-Newtonian fluids, particles settling in non-Newtonian fluids has received limited scientific attention. The simple case of two vertically aligned spheres settling in a thixotropic xanthan fluid is considered using solutions of xanthan + glycerol + water and 0.75 mm radius stainless steel spheres. Chaining phenomenon is observed where the trailing sphere velocity is increased due to a corridor of reduced viscosity created by the leading sphere. Our experimental methods are first validated against a Newtonian fluid of glycerol + water in which the sphere velocities remained equal. Using the fluid velocity induced by a single sphere, the two sphere velocities are approximated by Faxén's first law. In a non-Newtonian (thixotropic) xanthan fluid, a viscosity ratio is introduced to account for the reduced fluid viscosity encountered by the trailing sphere due to the slow structure recovery of the fluid after shear thinning. The viscosity ratio is an exponential decay function dependent on the time between spheres normalised by the fluid recovery time, a parameter which is experimentally determined. When the sphere-sphere separation is large, the viscosity ratio tends towards unity. The predicted settling velocities show good agreement with experimental data.

## 1. Introduction

Particle suspensions are ubiquitous in many industrial processes and the unique flow properties of non-Newtonian fluids may be advantageously exploited to process 'difficult' particles. For example, a shear dependent fluid can be used to resuspend/disperse particles when mixed at high shear stress ( $\tau$ ) thus lowering the fluid viscosity, and at low  $\tau$  the fluid viscosity is substantially higher and thus more favorable to maintain particles in suspension during transport (low  $\tau$ ) and/or storage ( $\tau \sim 0$ ). In the current study we consider the slow settling of particles in a quiescent non-Newtonian xanthan fluid.

In the settling of multiple monodisperse particles in non-Newtonian fluids, chaining of particles into vertical columns (regions of high particle concentration) has been reported, with regions of low particle concentration observed to provide routes for fluid backflow. Such behaviour occurs even when inertial effects are negligible [1–3]. Moreover, unlike a Newtonian fluid where the settling front moves at a constant velocity, in a shear thinning fluid, the settling front has a higher initial velocity, which slows as settling progresses [1].

The rheological properties of non-Newtonian fluids, including shear thinning, viscoelasticity and time-dependence, adds complexity to even simple systems. For example, for a single sphere settling with negligible inertia (low  $Re$ ), the terminal settling velocity in a Newtonian fluid is given by the Stokes equation. Classically, the shear rate ( $\dot{\gamma}$ ) of a sphere

settling in a non-Newtonian fluid is estimated as  $V/2r$  (e.g. [3–5]) or  $V/r$  (e.g. [6–9]), where  $V$  is the velocity of the sphere and  $r$  is the sphere radius. However, if the fluid viscosity determined from rheology at  $\dot{\gamma} = V/2r$  is used as an effective viscosity in the Stokes equation, the settling velocity for spheres settling in a shear thinning fluid is over-predicted [3,5]. It follows mathematically that the use of  $\dot{\gamma} = V/r$  would predict even higher settling velocities. In a non-time-dependent non-Newtonian fluid, there are many equations which attempt to predict the particle drag force. Many are based on simple rheological models such as power law or Bingham, but Chhabra notes in many cases the error in these calculations is no better than when using Newtonian equations [10]. Furthermore, time-dependent effects can be important in non-Newtonian fluids. It has been noted in several studies that the settling velocity of a sphere depends on the history of the fluid. Fluid history is manifested as both an increased terminal settling velocity over consecutive identical spheres [8,11], and a decreased terminal settling velocity as the time between spheres is increased [8,11,12].

The fluid flow around a single settling sphere at low  $Re$  is also modified from the Newtonian case. When a sphere settles in a Newtonian fluid the resultant flow pattern is reversible. In a non-Newtonian fluid, the most notable change is the break in fore-aft symmetry. The fluid velocity in front of a settling sphere is lower in a shear thinning fluid than a Newtonian fluid due to the increased fluid viscosity away from the sphere [6,13,14]. A negative wake is sometimes observed wherein

\* Corresponding authors.

E-mail addresses: [pmkab@leeds.ac.uk](mailto:pmkab@leeds.ac.uk) (K. Moseley), [d.harbottle@leeds.ac.uk](mailto:d.harbottle@leeds.ac.uk) (D. Harbottle).

<https://doi.org/10.1016/j.jnnfm.2019.104146>

Received 13 October 2018; Received in revised form 26 June 2019; Accepted 5 August 2019

Available online 7 August 2019

0377-0257/© 2019 The Authors. Published by Elsevier B.V. This is an open access article under the CC BY license. (<http://creativecommons.org/licenses/by/4.0/>)

the fluid velocity behind the sphere decays rapidly to a stagnation point and flows in the opposite direction to the settling sphere. In some viscoelastic fluids an extended wake is observed, where the fluid velocity behind the sphere decays over a longer distance than in a Newtonian fluid. It is generally agreed that the negative wake is formed from two competing forces, and that one of these is the extension of polymers in the region behind the sphere [13,15]. Experiments and simulations [7,16] have shown that when the polymer extension is large, the wake transitions to the extended wake form. The competing force to produce the negative wake is either shear [13] or normal stress [15,17].

When two identical vertically aligned spheres settle in a viscoelastic fluid, a critical distance,  $d_c$ , is observed where the spheres may converge or diverge [4,18,19]. Here we focus on the case where the spheres converge for an initial separation  $d_0 < d_c$  and the spheres move at a velocity equal to the single sphere velocity when  $d_0 > d_c$  [3,4]. Joseph et al. [4] concluded there are different mechanisms which can promote particle aggregation in viscoelastic fluids. Viscoelasticity and shear thinning with memory were both sufficient but not necessary to produce chained particles. A physical explanation for chaining in viscoelastic fluids was given by Phillips [20,21], whereby the streamlines envelop both particles and the normal stress difference causes the particles to converge. Joseph et al. [4] suggested a “corridor of reduced viscosity” to explain the chaining phenomenon in shear thinning fluids. The first particle settling causes a reduction in the fluid viscosity which does not immediately recover, hence subsequent spheres experience a lower fluid viscosity and settle faster, eventually leading to chaining. Hariharaputhiran et al. [22] suggested that the apparent reduction in viscosity is caused by network damage in the form of disentanglement of polymer molecules, which matched the timescales of recovery observed in their experiments ( $\sim 20$  min). The observed critical initial separation relates to the fully recovered fluid within experimental uncertainties, in agreement with other experimental and simulation studies [3,23].

Daugan et al. [3] studied the settling of two vertically aligned spheres in xanthan + glycerol + water solutions of varying concentrations and described the settling velocity using the Newtonian equation ( $V_1 = V_2 = V_S (1 + 3/2 \times r/d)$ ), where the Stokes settling velocity  $V_S$  was replaced by an experimental settling velocity, and the trailing sphere velocity ( $V_2$ ) increase was described by introducing a multiplication factor ( $V_2 = 1.2 \times V_1$  for all fluids). While this appears to fit the data for  $d_0 < d_c$ , it does not give the correct limiting conditions for two spheres in contact ( $V_1 = V_2$  at  $d = 2r$ , where  $r$  is the sphere radius and  $d$  is centre-to-centre separation), or at large separations ( $V_1 = V_2$  at  $d \rightarrow \infty$ ) [6,14], where  $V_1$  and  $V_2$  represent the velocities of the leading and trailing spheres, respectively.

Horsley et al. [12] studied the settling of identical spheres (pairs) of different diameter and density in a polyacrylamide (Floxit) solution. The authors found that curves of  $P \times \ln(V_2/V_1)$  against  $\ln(t^*)$  collapsed to a single curve for all spheres which they fitted using a polynomial ( $P$  is the plasticity index which can be obtained from the fluid rheogram and  $t^*$  is the dimensionless time gap). It was noted by the authors that there is an upper limit of  $\ln(t^*) = 6.4$ , above which  $P \times \ln(V_2/V_1)$  should be taken to equal zero [12]. However, for the limit of touching spheres, for which  $V_2/V_1$  should equal unity, the polynomial gives a number greater than zero for  $P \times \ln(V_2/V_1)$ .

The settling of identical spheres in polyacrylamide (Floxit) solution and the effect of sphere-sphere separation distance (time interval) was also considered by Gumulya et al. [5]. The authors proposed that the velocity of the trailing sphere was dependent on the product of a structure function and a time interval function, both in the form of power functions. The structure function ( $\alpha^N$ ) was based on the rheogram shape ratio  $\alpha$ , while the dimensionless time interval  $C_1(\dot{\gamma}t)^{C_2}$  was a function of the time interval ( $t$ ) and the representative shear rate ( $\dot{\gamma}$ ) with constant  $C_1$  and power  $C_2$ . Constants  $C_1$ ,  $C_2$ , and  $N$  were obtained from the experimental settling data. The authors noted that 87% of the experimental data was within 20% of the calculated velocity. They suggested that errors in calculating average velocities over a smaller distance resulted in

higher uncertainties at shorter time intervals [5]. It is worth noting that unlike the previous studies [3,12], the limits of time between particles,  $t \rightarrow 0$  and  $t \rightarrow \infty$ , give the correct value of  $V_2 = V_1$ . Additionally, for a Newtonian fluid with  $\alpha = 1$ ,  $V_2 = V_1$  as expected.

Daugan et al. [3], Horsley et al. [12] and Gumulya et al. [5] accounted for time dependence by introducing constants which were evaluated using experimental data. Yu et al. [23] used numerical methods and introduced a structure parameter  $\lambda$  (where  $\lambda = 1$  for an undisturbed fluid and  $\lambda = 0$  when the structure is completely destroyed). The authors used the structure parameter as part of a thixotropic model to describe the fluid viscosity recovery after shear thinning. The authors note that the settling behaviour is similar to that observed by Daugan et al. [3], but quantitative comparisons were not made. Gumulya et al. [24] improved their model using a similar method to Yu et al. [23]. Transient rheology was measured, from which they determined  $\theta$ , the recovery time of the fluid. The structure parameter incorporated  $\theta$  and the shear rate dependence of a shear thinning fluid, which is constant and equal to unity for a Newtonian fluid. However, the authors ultimately rely on fitting a polynomial to the data to account for the difference between the shear rate to give an effective viscosity experienced by the settling sphere, and the steady state shear rate from the sphere shear stress.

In the current study we consider the interactions between two vertically aligned spheres in a Newtonian fluid to inform our prediction of settling velocities in non-Newtonian fluids. In a Newtonian fluid, spheres settle at equal velocities ( $V_1 = V_2$ ) depending on the centre-to-centre separation. As the separation decreases, the velocity of both spheres increases due to hydrodynamic interactions [25]. We use Faxén’s first law to approximate the sphere velocities in Newtonian fluids, in terms of the fluid velocity caused by the settling of a single sphere, and use this as the foundation for our non-Newtonian model. The fluid velocity term readily allows the inclusion of the modified non-Newtonian fluid behaviour (lower fluid velocity in front of the sphere caused by shear thinning and modified wake behaviour caused by viscoelasticity and extensional stresses). The transient nature (thixotropy) of the fluid viscosity in the corridor of reduced viscosity is incorporated by introducing a viscosity ratio term. Experimental data of two spheres settling in xanthan + glycerol + water solutions is used for validation of the method.

## 2. Materials and experimental methods

### 2.1. Fluid preparation and characterization

Xanthan gum (Sigma Aldrich, UK) is a high molecular weight polysaccharide gum. Xanthan solutions were prepared by first mixing xanthan powder with glycerol (Fisher Scientific, UK) by hand until it appeared well dispersed then adding Milli-Q water (resistivity = 18.2 M $\Omega$  cm) to produce a 3:2 mass ratio of glycerol to water and 0.25 wt% xanthan. The overall solution concentration was 0.25 wt% xanthan, 59.85 wt% glycerol and 39.9 wt% water. The solution was mixed using a magnetic stirrer for 30 min at 700 rpm, inverting every few minutes to enhance mixing throughout the entire volume. The sequence of addition helped create a homogeneous mixture since xanthan gum tended to clump together when added directly to Milli-Q water and was difficult to disperse in the large (800 mL) total volume of solution. The final xanthan solution was left to fully dissolve at room temperature ( $T = 22 \pm 5$  °C) for 30 days which ensured all entrained air bubbles were removed before rheological and settling tests were conducted. All experiments were conducted within 90 days. No change was observed in the solution properties over this time and rheological measurements taken at 30 and 90 days showed good agreement. The density of the final xanthan solution was 1162 kg m $^{-3}$ . For comparison, a Newtonian fluid of 95 vol% glycerol and 5 vol% Milli-Q water mixture was prepared on the first day of use and all experiments were completed within one week. The density of the Newtonian solution was 1240 kg m $^{-3}$  and the viscosity was 0.461 Pa s ( $R^2 = 0.9999$ ). The composition of the Newtonian fluid was chosen such that the settling velocity of a 1.5 mm (diameter)

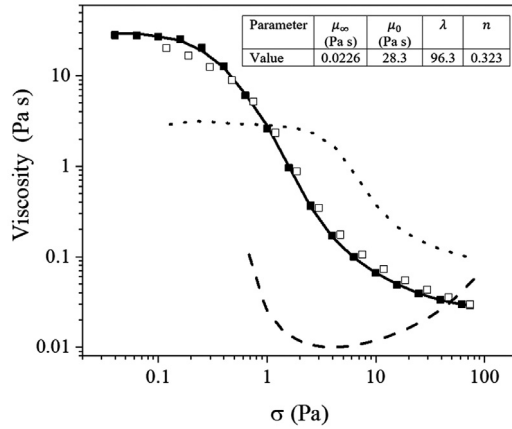


**Fig. 1.** Shear thinning behaviour of the xanthan solution (0.25 wt% xanthan, 59.85 wt% glycerol, 39.9 wt% water) with fluid viscosity measured over 30 s averaging time after 30 s equilibrium time per measurement point. Open and closed symbols represent the stress sweep increase and decrease respectively. Solid line – Carreau model (Eq. (1)) fit to the increasing stress sweep data. Dot and dash lines show the respective increasing and decreasing flow ramps taken over 10 s.

stainless steel sphere was similar in both the Newtonian (glycerol and water) and non-Newtonian (xanthan, glycerol and water) fluids. The settling velocity was  $17.0 \text{ mm s}^{-1}$  in the Newtonian fluid and  $13.5 \text{ mm s}^{-1}$  in the non-Newtonian xanthan fluid.

All rheology measurements were made at  $24^\circ\text{C}$  using a TA Instruments DHR-2 rheometer. This temperature matched the room temperature for the settling experiments. A  $40 \text{ mm } 2^\circ$  steel cone and Peltier plate geometry with a truncation of  $52 \mu\text{m}$  was used. Fig. 1 shows the steady-state shear viscosity of the xanthan solution as a function of shear stress over the range  $0.1\text{--}100 \text{ Pa}$ . Closed and open symbols represent the fluid viscosity as the applied stress is increased and decreased, respectively. After the samples were loaded, a wait time of  $180 \text{ s}$  was applied to allow the fluid viscosity to recover following the stresses caused during sample loading. For each data point,  $30 \text{ s}$  was allowed for the system to reach steady state before data was collected following a further  $30 \text{ s}$  of averaging. The similarity between the increasing and decreasing stress flow curves suggests that steady state was approximately achieved. We will refer to the increasing stress sweep as the quasi-steady state curve.

The Carreau model [26] (Eq. (1)), with the model parameters shown in the inset table of Fig. 1, was used to describe the measured quasi-steady state xanthan solution viscosity ( $\mu$ ) as a function of shear stress ( $R^2 = 0.9998$  for ramp-up):

$$\frac{\mu - \mu_\infty}{\mu_0 - \mu_\infty} = (1 + (\lambda\dot{\gamma})^2)^{\frac{n-1}{2}} \quad (1)$$

where  $\mu_\infty$  and  $\mu_0$  are the infinite shear viscosity and zero shear viscosity, respectively.  $\lambda$  is the consistency index and  $n$  the rate index.

For comparison, the dot line shows the fluid viscosity when the stress was increased linearly from  $0.1$  to  $100 \text{ Pa}$  over  $10 \text{ s}$ . The dash line shows a decreasing stress ramp which followed immediately from the ramp-up and was also measured over the same stress range and timescale. These measurements were taken after  $60 \text{ s}$  pre-shear at  $0.1 \text{ Pa}$ . Hysteresis, suggesting thixotropy, is clearly shown in the stress ramp data. The ramp-up viscosity shows a plateau at low stress with the fluid viscosity lower than the quasi-steady state stress sweep, suggesting the fluid structure was not fully developed at the start of the test following the pre-shear protocol. With increasing stress, the fluid viscosity measured during the  $10 \text{ s}$  ramp-up is higher than the quasi-steady state stress sweep measurements, suggesting more fluid structure remains at short times and therefore the fluid structure requires extended time to break down.

Fig. 2 shows the viscosity recovery of the xanthan solution at  $0.3 \text{ Pa}$  after a period of stress (specified in the figure). At  $300 \text{ s}$  the viscosity is still increasing and steady state is not reached. The importance of

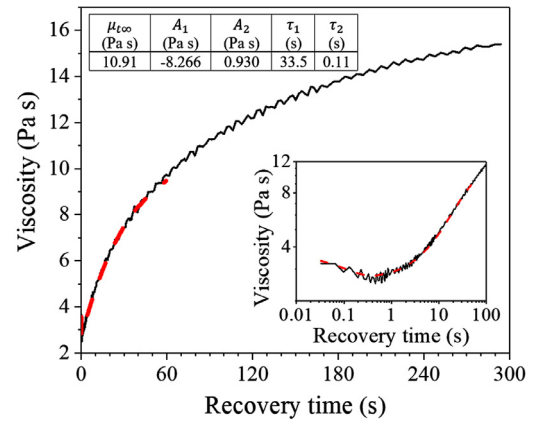


**Fig. 2.** Viscosity recovery of the xanthan solution measured at  $0.3 \text{ Pa}$ . First a shear stress of  $0.3 \text{ Pa}$  was applied for  $180 \text{ s}$  followed by a linear ramp-up to  $10.2 \text{ Pa}$  and ramp-down to  $0.3 \text{ Pa}$  over a period of  $4 \text{ s}$  (mimicking the pre-shear stress protocol of the xanthan solution in the settling column – data not shown). After a hold time of  $600 \text{ s}$ , the stress was linearly ramped up to  $5.4 \text{ Pa}$  and ramped down to  $0.3 \text{ Pa}$  over a period of  $4 \text{ s}$  (mimicking the shear stress exhibited by a single settling sphere – data not shown). The fluid viscosity recovery over  $300 \text{ s}$  was then measured at  $0.3 \text{ Pa}$  (solid line). Fitting parameters and values for Eq. (2). (dash line) are shown inset. Inset figure shows the same data on a log-log scale to clearly show features at short timescales.

measuring the fluid viscosity recovery time was evidenced during preliminary testing when a single  $1.5 \text{ mm}$  stainless steel sphere, released approximately  $4 \text{ h}$  after the initial sphere, was observed to migrate laterally to the position of the previous sphere path. Therefore, to attain reproducible measurements, two  $2 \text{ mm}$  diameter spheres (apparent stress =  $10.2 \text{ Pa}$ ) were first dropped through the fluid as a pre-shear protocol followed by a  $600 \pm 5 \text{ s}$  recovery period. It should be noted that experimental data where horizontal alignment of the settling sphere was greater than  $12 \text{ px}$  from the pre-shear sphere at the same position was discarded and not further analysed. The long recovery time shown in Fig. 2 is incongruent to the  $60 \text{ s}$  step time data presented in Fig. 1, as during the decreasing stress sweep the time between  $\tau = 5.4 \text{ Pa}$  and  $\tau = 0.3 \text{ Pa}$  (shear stress limits applied in Fig. 2) is  $\sim 5 \text{ min}$  in Fig. 1 and in Fig. 2. At  $t > 5 \text{ min}$ , the viscosity change with time is negligible compared to the initial rate of change, therefore the condition of quasi-steady state is reasonable.

The rheological procedure to study the fluid viscosity recovery after a period of high shear was designed to replicate the stresses experienced by the fluid during a sphere settling experiment. A pre-shear of  $0.3 \text{ Pa}$  for  $180 \text{ s}$  allowed some recovery of the fluid viscosity after sample loading. A  $2 \text{ s}$  linear ramp-up to  $10.2 \text{ Pa}$  and ramp-down to  $0.3 \text{ Pa}$  replicates the stress of two  $2 \text{ mm}$  stainless steel spheres settling through the fluid. A wait time of  $600 \text{ s}$  was used in the experiments, followed by the settling of a  $1.5 \text{ mm}$  sphere. This was replicated using another ramp-up and ramp-down over  $4 \text{ s}$  to a peak of  $5.4 \text{ Pa}$ . The fluid viscosity recovery was recorded at  $0.3 \text{ Pa}$  at  $1 \text{ s}$  intervals and is shown in Fig. 2. A stress of  $0.3 \text{ Pa}$  was used as the baseline as a compromise between a stress in the zero shear region and displacement above the instrument sensitivity limits when short ( $1 \text{ s}$ ) measurement intervals were used. An increase in fluid viscosity with time is clearly seen following the decreasing stress step change (thixotropy). An exponential decay function (Eq. (2), dash line in Fig. 2), was used to fit the data when  $t < 60 \text{ s}$  ( $R^2 = 0.997$ ), and the fitting parameters are given in the inset table in Fig. 2. The region  $t < 60 \text{ s}$  was selected as all settling tests were within this region. The exponential decay function used was:

$$\mu(t) = \mu_{t\infty} + A_1 e^{-\frac{t}{\tau_1}} + A_2 e^{-\frac{t}{\tau_2}} \quad (2)$$

Fig. 2. (inset) shows the same viscosity recovery on a log-log scale. A decrease in viscosity is seen at short timescales ( $t < 1 \text{ s}$ ). This is consistent with viscoelastic fluid behaviour [27]. The time constants  $\tau_1$  ( $33.5 \text{ s}$ ) and

$\tau_2$  (0.11 s) in Eq. (2) are indicative of the relative timescales of the structure (thixotropic) and elastic recovery times. Small amplitude oscillatory shear (SAOS) measurements gave a characteristic elastic timescale in the order of 10 s (1/crossover frequency [28]) (Fig. A1), however, the small deformations in SAOS may not be representative as the structure is not destroyed [29]. Large amplitude oscillatory shear (LAOS) measurements were made on a representative (0.25 wt% xanthan, 59.85 wt% glycerol, 39.9 wt% water) fluid and showed that the energy dissipated increases with increasing strain amplitude while both elastic and viscous contributions become increasingly non-linear (for more information see Appendix A).

## 2.2. Settling spheres

A settling column of dimensions 300 mm  $\times$  50 mm  $\times$  50 mm ( $h \times w \times l$ ) with one end closed (VitroCom) was used throughout the study. The spheres were made from hardened 420 stainless steel (Ital ball) with a diameter of  $1.5 \pm 0.0381$  mm and density =  $7790 \text{ kg m}^{-3}$ . The spheres were grade 100 with a maximum surface roughness of  $0.127 \mu\text{m}$ . The spheres were washed in a dilute (2 vol%) Decon@90 solution, rinsed thoroughly with Milli-Q water and dried prior to use. A custom-made sphere release mechanism was used to accurately control the sphere release timings. The device consisted of a 50 mm long, 2.5 mm I.D. glass tube vertically orientated and centred on the settling column. The tube was used to hold the spheres in vertical alignment prior to release. The 2.5 mm I.D. tube was chosen to minimize the lateral movement of 1.5 mm and 2 mm spheres. Two electromagnets were positioned on the outside wall of the 2.5 mm glass tube to hold the spheres prior to release. The electromagnets were approximately 5 mm and 8 mm from the end of the glass tube and were operated independently to control the sphere release time interval. Through continued use, the electromagnets appeared to weakly magnetise the spheres. Since the magnetism could affect the interaction between settling spheres, the contribution was assessed and shown to be negligible (i.e. no interaction) when the spheres were  $\geq 1$  mm apart (visual assessment when spheres were placed on a level glass substrate). In addition, a second release mechanism without electromagnets was used to validate the settling rates at small separations ( $d/r < 40$ ). The second release mechanism was of a rotary style, where the spheres were placed in holes drilled in an acrylic circle which rotated until the sphere aligned with a hole in the base plate, releasing the sphere into the fluid. New spheres (non-magnetized) were used and the measured velocities were within the scatter of the data collected using the electromagnet release mechanism. The second release mechanism was not used in the study because alignment of the two spheres was less reliable and there was less flexibility for release intervals due to the size limitation of the rotating circle.

The time interval between releasing the two spheres was varied from 0.5 to 8.5 s in 0.5 s increments. Time intervals were limited to 0.5 s by the I/O device used (National Instruments USB-6001) which led to some gaps in the data, see Figs. 5 and 8. The upper limit of the time interval was set by the 100 mm field of view of the camera; both spheres must be visible in the frame of capture to precisely measure the distance between the spheres.

Fig. 3 shows the coordinate system with the axis centred on the first sphere (radius  $r$ ), and the sphere settling along the  $Z$  axis at a velocity  $V$ . Positive values of  $Z$  are opposite to the direction of sphere settling (i.e. behind the centre of the sphere). The fluid velocity is axisymmetric perpendicular to the  $Z$  axis. Only the fluid velocity along the vertical centreline ( $\rho = 0$ ) was considered in this study. Any experiments where the two settling spheres were not vertically aligned were discarded.

Two methods were used to analyse the settling spheres: (i) measuring the sphere settling velocity using a simple camera set up, and (ii) measuring the fluid velocity around the settling spheres using particle imaging velocimetry (PIV). Both methods used the settling column and release mechanism detailed above.

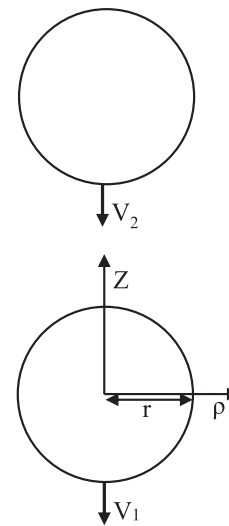


Fig. 3. Cylindrical coordinate system centred on the sphere. The longitudinal ( $Z$ ) axis is the line of interest, along which the sphere settles. The radial direction is denoted  $\rho$  and the radial angle is not required due to symmetry. The radius of the sphere and the settling velocity are given by  $r$  and  $V$ , respectively.

- i) **Sphere velocity:** Images of the settling spheres were captured using a Point Grey Chameleon3 camera. An optimum frame rate of 30 fps was used to provide both good exposure so that the settling spheres were not blurred, and a sufficient number of images were collected for subsequent analysis. A MATLAB® script was used to determine the sphere locations using peak analysis and tracked the sphere position as a function of time. The time and position data were used to calculate the sphere settling velocity over 9 frames (0.3 s) which was found to be a compromise between minimising noise and retaining resolution. The sphere separation corresponding to the measured velocity was determined using the sphere locations on the middle (5th) frame.
- ii) **Fluid velocity:** PIV was used to measure the fluid velocity field around the settling sphere. Fluorescent tracer particles (1–20  $\mu\text{m}$  PPMA-Rhodamine B) were added to the test fluid at a concentration of 25 mg in 100  $\mu\text{L}$  of Milli-Q water to 1 L of test fluid. The density of the tracer particles was very similar to the test fluid ( $1.19 \text{ kg m}^{-3}$ ) and the tracer particles did not noticeably settle during the duration of the experiment. A vertical laser sheet (Dantec DualPower 65-15) was used to illuminate the tracer particles in the plane of interest. The laser sheet was centred on the settling sphere and aligned perpendicularly to the camera (Dantec FlowSense EO 2M). When the laser and sphere were aligned correctly, a shadow was observed across the image. In cases where the alignment was poor the results were not considered. The captured images were processed with the Dantec DynamicStudio (v3.41) software using the adaptive PIV analysis. Interrogation area grid sizes between 8 and 128 px were selected to allow for an uneven distribution of tracer particles. No vector analysis was used at this stage to preserve the data and ensure that interesting features were not removed. The velocity vector fields were recorded and averaged over 23 (Newtonian fluid) and 35 (non-Newtonian fluid) frames.

## 3. Results and discussion

### 3.1. Settling in a Newtonian fluid

The dynamics of slow settling spheres in Newtonian fluids are relatively well understood, thus we used a Newtonian fluid to validate the experimental procedures and to provide a basis for comparison. The

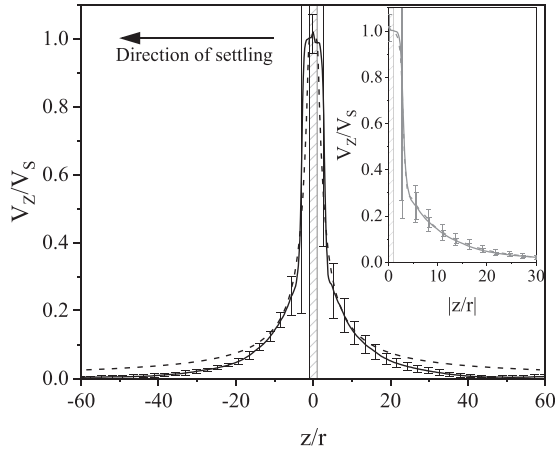


**Fig. 4.** Fluid velocity ( $V_Z$ ) around a single sphere settling at  $V_S$  as a function of distance along the  $Z$  axis. The sphere centre is located at  $z/r=0$ .  $z/r < 0$  is the fluid ahead of the sphere and  $z/r > 0$  is the fluid behind the sphere. The solid line represents the measured (PIV) fluid velocity caused by a 1.5 mm (diameter) stainless steel sphere settling in a Newtonian fluid (glycerol 95 vol% + water 5 vol%). The dash line represents the velocity as predicted by the Stokes stream function (Eq. (7)). Shaded region at  $|z/r| \leq 1$  indicates the sphere location and thus a fluid velocity is not applicable. Inset – an overlay of fluid velocity ahead (solid) and behind (dash) the settling sphere.

terminal velocity of a single sphere is given by the solution of the Navier–Stokes equations. The general solution for a single sphere with negligible inertia is given by Stokes' law (Eq. (3)) when  $K_1 = 1$ :

$$V_S = \frac{2(\rho_S - \rho_F)gr^2}{9\mu K_1} \quad (4)$$

$$K_1 = \frac{1 - 0.75857\left(\frac{r}{R}\right)^5}{1 - 2.1050\left(\frac{r}{R}\right) + 2.0865\left(\frac{r}{R}\right)^3 + 0.72603\left(\frac{r}{R}\right)^6} \quad (4)$$

where  $V_S$  is the Stokes velocity,  $\rho_S$  and  $\rho_F$  are the sphere and fluid density respectively,  $g$  the acceleration due to gravity ( $9.81 \text{ m s}^{-2}$ ),  $r$  the sphere radius and  $\mu$  the fluid viscosity.  $K_1$  is a wall correction factor for a sphere settling in a cylinder of radius  $R$  and infinite length [30,31]. Experimentally, the settling velocity of a  $r = 0.75 \text{ mm}$  stainless steel sphere was  $17.0 \pm 0.12 \text{ mm s}^{-1}$ . Using Eq. (3) and  $\rho_S = 7790 \text{ kg m}^{-3}$ ,  $\rho_F = 1250 \text{ kg m}^{-3}$ ,  $r = 0.75 \text{ mm}$  and  $\mu = 0.461 \text{ Pa s}$ , the Stokes velocity ( $V_S$ ) was calculated to be  $17.4 \text{ mm s}^{-1}$ . Including the wall correction factor gives  $V_S = 16.9 \text{ mm s}^{-1}$ , which is within the uncertainty of the measurement. This suggests some wall effects may be present although the experimental settling velocity is within 2.5% of the Stokes velocity so the contribution may be considered small.

A settling sphere induces fluid flow which is axisymmetric about the axis of settling. The fluid velocity field (Eq. (5)) caused by a sphere settling in a Newtonian fluid at low  $Re$  can be determined using the Stokes stream function,  $\psi$  (Eq. (6)), where  $\alpha = z^2 + \rho^2$  [32]. The fluid velocity profile along the  $Z$  axis (the vertical centreline where  $\rho = 0$ ),  $V_Z$ , is given in terms of the distance from the sphere centre ( $z$ ), the sphere radius ( $r$ ), and the sphere velocity ( $V_S$ ) in Eq. (7). Fig. 4 shows  $V_Z$  normalised by the sphere velocity,  $V_S$ , versus the distance along the  $Z$  axis, normalised by the sphere radius,  $z/r$ . Eq. (7) is shown by the dash line and the solid line represents the experimental (PIV) fluid velocity along the  $Z$  axis caused by a 1.5 mm (diameter) stainless steel sphere settling in a glycerol-water (95 vol% + 5 vol%) solution.

$$V_Z = \frac{1}{\rho} \frac{\partial \psi}{\partial \rho} \quad (5)$$

$$\psi = \frac{3}{4} V_S r \rho^2 \left( \alpha^{-\frac{1}{2}} - \frac{1}{3} r^2 \alpha^{-\frac{3}{2}} \right) \quad (6)$$

$$V_Z = V_S \left( \frac{3}{2} \frac{r}{z} - \frac{1}{2} \frac{r^3}{z^3} \right) \text{ for } \rho = 0 \quad (7)$$

Here, the Stokes stream function ( $\psi$ ) is given in cylindrical coordinates centred on the sphere.  $z$  is the longitudinal distance, and  $\rho$  the radial distance.

The PIV and Stokes stream function fluid velocities are in good agreement and show the same general shape (Fig. 4). The fluid velocity is at a maximum at the edge of the sphere ( $|z/r| = 1$ ) and decays monotonically to zero for increasing values of  $|z/r|$ . For  $|z/r| < 10$ , the fluid velocity predicted by the Stokes stream function (Eq. (7)) is within experimental uncertainty of the PIV data (1 standard deviation). Note the large uncertainty in the velocity at small distances from the sphere ( $1 < |z/r| < 3.5$ ) which results from difficulty in tracking the PIV tracer particles in the region of a high velocity gradient, and low image contrast due to reflection of the PIV laser on the steel spheres. At larger distances the measured PIV fluid velocity is over-predicted by the Stokes stream function up to  $0.03V_S$ . This reduction in fluid velocity has been reported to occur when the column radius is decreased and can be attributed to wall effects as discussed earlier [7].

Fig. 4 (inset) shows the similarity between the PIV fluid velocity in front of and behind the settling sphere. The error bars show 1 standard deviation of the fluid velocity in front of the sphere, suggesting that the fluid velocity is not significantly different and can be considered symmetric. This suggests that inertial effects can be considered negligible for single sphere settling.

The motion of two spheres settling along their line of centres was solved by Stimson and Jeffrey [33] who used the Stokes stream function (Eq. (6)) to determine the forces exerted upon the spheres. This has been approximated using the method of reflections with good accuracy [30]. The velocity of sphere  $i$  after the first reflection can be obtained from Faxén's first law [34,35] (Eq. (8)).

$$V_i = V_{S(i)} + \left( 1 + \frac{r^2}{6} \nabla^2 \right) V_{Z(3-i)} \Big|_{z=z_i} \text{ for } i = 1, 2 \quad (8)$$

The velocity of sphere  $i$  ( $V_i$ ) is the sum of the single sphere velocity of sphere  $i$  plus the velocity of the fluid disturbance caused by the neighbouring sphere  $V_{Z(3-i)}$  at the location of sphere  $i$  ( $z = z_i$ ). Where the Laplacian of  $V_Z$  along the  $Z$  axis ( $\rho = 0$ ), assuming radial symmetry is given by Eq. (9), and  $z$  and  $\rho$  are the longitudinal and radial directions (see Fig. 3).

$$\nabla^2 V_{Z(i)} = 2 \frac{\partial^2 V_Z}{\partial \rho^2} + \frac{\partial^2 V_Z}{\partial z^2} \text{ for } \rho = 0 \quad (9)$$

Eqs. (8) and (9) may be applied to the fluid velocity derived from the Stokes stream function (Eqs. (5) and (6)) or the experimentally determined fluid velocity by PIV. The symmetry of the Newtonian fluid velocity along the  $Z$  axis predicts  $V_1 = V_2$ .

Fig. 5 shows the velocity of two spheres ( $V_1$  and  $V_2$ ) settling in a Newtonian fluid normalised by the single sphere velocity ( $V_S$ ) as a function of the normalised centre-to-centre separation ( $d/r$ ), where  $V_1$  is the leading sphere (square symbol) and  $V_2$  the trailing sphere (circle symbol). The settling velocity of each sphere was measured directly from the sphere settling experiments at different separations ( $d$ ). The sparse data is due to the 0.5 s release interval restriction described earlier. An average is shown at each separation and the error bars represent 1 standard deviation from the mean. There is some scatter in the data which may be due to distortion of the camera lens, small temperature fluctuations or small inaccuracies in the camera frame rate and sphere location. The settling velocity was calculated over 9 frames in an attempt to minimise the effect of these fluctuations. Additionally, error in calculating the single sphere velocity,  $V_S$ , would cause the experimental normalised sphere velocity curve to shift vertically which may explain the normalised velocity of less than 1 when  $d/r > 90$ .

The lines shown in Fig. 5. represent the sphere velocities calculated from Eqs. (8) and (9) using different methods to determine the fluid

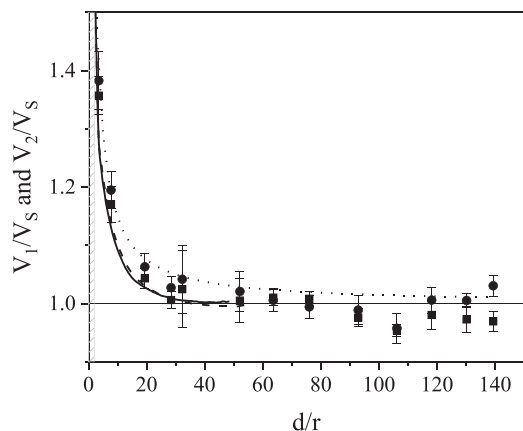


**Fig. 5.** Normalized sphere velocity of the leading ( $V_1$ ) and trailing ( $V_2$ ) spheres when two vertically aligned spheres settle in a Newtonian fluid (glycerol 95 vol% + water 5 vol%). Symbols: square – leading sphere; circle – trailing sphere. Lines – sphere velocities calculated using Eqs. (8) and (9) using different methods to determine the fluid velocity,  $V_z$ . Dot line –  $V_z$  calculated from Stokes stream function; dash and solid lines – leading and trailing sphere velocities calculated from PIV, respectively. Shaded region,  $d/r < 2$ , corresponds to separations less than two contacting spheres.

velocity  $V_z$ . The dot line uses the Stokes stream function (Eqs. (5) and (6)) to calculate the fluid velocity,  $V_z$  ( $V_1 = V_2$  due to symmetry), while the dash and solid lines show the leading and trailing sphere velocities, respectively, as calculated from the fluid velocity around a settling single sphere measured by PIV. The calculated sphere velocities are slightly lower than the Stokes stream function sphere velocities for all  $d/r$  as a direct consequence of the lower fluid velocity as shown in Fig. 4.

Eq. (8) shows that with inertial effects neglected, the velocity of the leading sphere ( $V_1$ ) is equal to the velocity of the trailing sphere ( $V_2$ ) due to fore-aft symmetry of the fluid velocity field caused by a single sphere settling. Directly measuring the sphere velocities (symbols), it is noted that the average velocity of the trailing sphere,  $V_2$  (circles), is slightly higher than the velocity of the leading sphere,  $V_1$  (squares), however the velocities remain within 1 standard deviation except at  $d/r = 140$ , which is within 2 standard deviations, so this difference may not be significant.

Good agreement between the directly measured sphere velocities, the sphere velocities calculated using Stokes stream function and the sphere velocities determined from fluid and single sphere velocities is shown for most values of  $d/r$ , with sphere velocities mostly within 1 standard deviation of the average measured velocity. We conclude that the use of Faxén's first law (Eq. (8)) and the fluid velocity measured by PIV, produces an adequate representation of the experimental sphere velocities of two spheres settling with vertical alignment at low  $Re$  in a Newtonian fluid (95 vol% glycerol + 5 vol% water).

### 3.2. Settling in a non-Newtonian xanthan fluid

The motion of two vertically aligned spheres settling along their line of centres in a non-Newtonian (thixotropic, shear thinning, viscoelastic) fluid is not well understood. The situation is complicated by the transient nature of the viscosity in a thixotropic fluid. We extend the method previously outlined (Section 3.1) to determine the velocity of two spheres settling with vertical alignment in a non-Newtonian xanthan fluid. Eq. (8) is first considered. There are two main differences between two spheres settling in Newtonian and non-Newtonian (thixotropic, shear thinning, viscoelastic) fluids: (i) the fluid velocity profile resulting from a settling sphere differs significantly; and (ii) the thixotropic shear thinning behaviour of the non-Newtonian fluid causes the trailing sphere to settle at a higher velocity due to a "corridor of reduced viscosity".

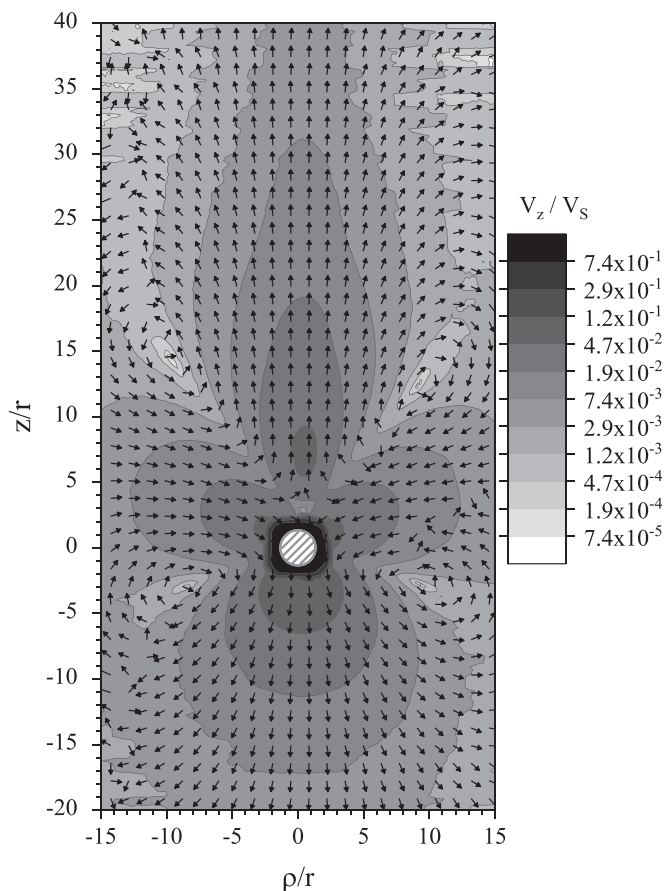


**Fig. 6.** Fluid velocity field around a 0.75 mm ( $r$ ) stainless steel sphere (sphere location identified by the shaded (lines) region) settling in a non-Newtonian fluid (0.25 wt% xanthan, 59.85 wt% glycerol, 39.9 wt% water). Contour map shows the fluid velocity magnitude and arrows indicate the fluid direction. A negative wake is clearly observed behind the sphere ( $z/r > 0$ ).

- i) **Fluid velocity:** The fluid velocity profile around a single sphere settling in a non-Newtonian xanthan fluid no longer shows fore-aft symmetry and a negative wake is observed when shear thinning and viscoelasticity are present [6,36,37]. Fig. 6 shows the fluid velocity caused by a 0.75 mm ( $r$ ) stainless steel sphere settling in a non-Newtonian fluid (0.25 wt% xanthan gum + 59.85 wt% glycerol + 39.9 wt% water) measured by PIV and averaged over 35 images. The sphere is identified by the shaded (lines) region centred at (0, 0). The measured fluid velocity field is visually similar to the velocity fields previously reported for a variety of different viscoelastic fluids [6,36,37]. This is expected as the non-Newtonian xanthan fluid exhibits viscoelasticity.

The settling velocity of a single 1.5 mm (diameter) stainless steel sphere in a non-Newtonian fluid (0.25 wt% xanthan, 59.85 wt% glycerol, 39.9 wt% water) was found to be  $13.5 \pm 0.15 \text{ m s}^{-1}$ . From Stokes' law the equivalent Newtonian viscosity is  $0.602 \text{ Pa s}$  and the particle Reynolds number is 0.039. This equivalent viscosity is higher than the viscosity predicted by either  $\dot{\gamma} = V/2r$  ( $\mu = 0.313 \text{ Pa s}$ ) or  $\dot{\gamma} = V/r$  ( $\mu = 0.204 \text{ Pa s}$ ). This is consistent with other work [3,5] and is conceptually compatible with a thixotropic fluid where the structure takes time to be destroyed when a stress is applied.

Fig. 7 compares the measured (PIV) fluid velocities along the  $Z$  axis caused by a single sphere settling in a non-Newtonian xanthan fluid (solid line) and Newtonian fluid (dot line). The Newtonian fluid velocities determined from the Stokes stream function (Eq. (7)) are shown by the dash line. The settling sphere is centred at  $z/r = 0$ . PIV measurements in both Newtonian and non-Newtonian fluids show poor resolution of

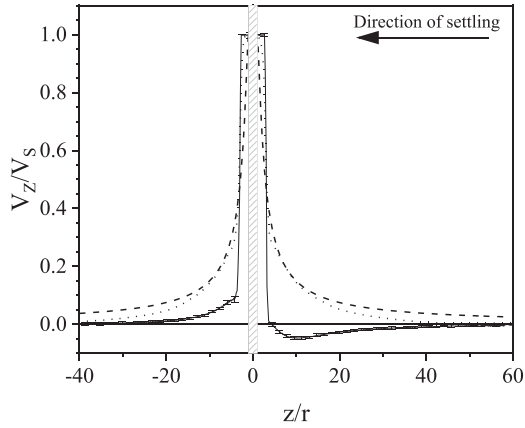


**Fig. 7.** Fluid velocity profile in front of ( $z/r < -1$ ) and behind ( $z/r > 1$ ) a single sphere settling in a non-Newtonian xanthan fluid (solid line) normalised by the sphere velocity ( $V_z/V_s$ ) as a function of the normalized distance ( $z/r$ ). The sphere is centred at  $z/r = 0$ . The negative wake behind the sphere is clearly shown. The error bars represent 1 standard deviation. The fluid velocity in a Newtonian fluid is shown for comparison, with the fluid velocity derived from the Stokes stream function (Eq. (7)) and PIV measurements shown by the dash and dot lines, respectively. Shaded region at  $|z/r| \leq 1$  indicates the sphere location and thus a fluid velocity is not applicable.

the fluid velocity at small values of  $|z/r| < 3.5$  due to the high velocity gradient in this region and reflection of the PIV laser from the sphere's surface.

Fore-aft asymmetry is clearly shown in the non-Newtonian xanthan fluid (solid line). In front of the sphere ( $z/r < -1$ ), the fluid velocity profile shows a similar shape to a Newtonian fluid (dot line); the velocity decays monotonically to zero with increasing distance from the sphere. The fluid velocity behind the sphere ( $z/r > 1$ ) decreases rapidly away from the sphere, becoming negative at  $z/r \sim 3.5$  until a maximum negative velocity ( $V_{neg}$ ) is reached at  $z/r \sim 10$ . Finally, for  $z/r > 10$ , the fluid velocity decays monotonically to zero.

For  $z/r < -1$ , the fluid velocity profile is qualitatively similar to that of a Newtonian fluid, however,  $V_z/V_s$  is smaller for the non-Newtonian xanthan fluid compared to the Newtonian fluid due to the shear thinning nature of the non-Newtonian fluid. As the distance from the sphere increases the shear rate decreases. In a shear thinning fluid, the fluid viscosity increases with decreasing shear rate, and thus the fluid velocity decreases. We do not expect wall effects to be significant in a shear thinning fluid where the ratio of sphere diameter-to-column width ( $2r/L$ ) is 0.03. Bisgaard [11] studied the negative wake for sphere-to-column radius ratios ( $r/R$ ) of between 0.04 and 0.14 and observed that the ratio of maximum negative wake velocity to sphere velocity ( $V_{neg}/V_s$ ) was approximately constant throughout, suggesting that wall effects were minimal. When larger radius ratios of  $r/R = 0.25, 0.50$  and  $0.75$  were considered experimentally by Sigli and Coutanceau [7],  $|V_{neg}/V_s|$  increased with increasing  $r/R$ . The effect of  $r/R$  on the shape of the velocity profile ahead of the sphere was not reported. Harlen [13] investigated the negative wake using a numerical simulation and  $r/R = 0.1-0.25$ . The same trend of increasing  $|V_{neg}/V_s|$  with increasing  $r/R$  was observed.

- ii) *Non-Newtonian xanthan fluid viscosity*: When two spheres settle with vertical alignment in a thixotropic shear thinning fluid, the trailing sphere settles at a higher velocity because the leading sphere stresses the fluid to decrease the viscosity (shear thinning) which then takes time to recover (thixotropy), thus the trailing sphere experiences a lower fluid viscosity. To capture this behaviour, the reduced viscosity experienced by the trailing sphere needs to be accounted for. We assume (i) the leading sphere velocity is equal to the single sphere velocity before interactions (fluid) are accounted for, as is the case for a Newtonian fluid, (ii) the trailing sphere velocity can be simply multiplied by a

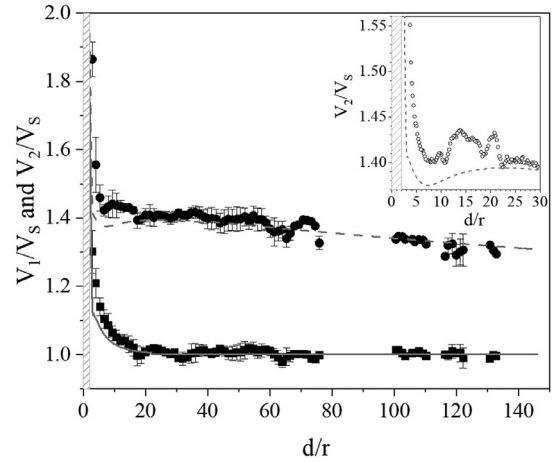


**Fig. 8.** Leading (square) and trailing (circle) sphere velocity as a function of separation distance ( $d/r$ ). Shaded region,  $d/r < 2$ , corresponds to separations less than two contacting spheres. Inset – single dataset (open symbol) showing the trailing sphere velocity,  $V_2/V_s$ , for  $d/r < 30$ . Fluid: 0.25 wt% xanthan, 59.85 wt% glycerol, 39.9 wt% water. Sphere velocities calculated from PIV Eqs. (10) - (12) are shown by the solid line (leading sphere) and dash line (trailing sphere).

viscosity ratio ( $\frac{\mu_s}{\mu_2}$ ) before hydrodynamic interactions are calculated, to account for the reduced viscosity the trailing sphere experiences due to thixotropy (Arigo and McKinley [9] found that for spheres of different size and density settling in a viscoelastic fluid exhibiting a negative wake, the normalised  $V_z/V_s$  against  $z/r$  curves collapsed to a single curve [9]), and (iii) the fluid viscosity decrease due to shear thinning is not significant (particularly at large sphere-sphere separations). Therefore, Eq. (8) in a Newtonian fluid becomes Eqs. (10) and (11), for the leading and trailing spheres respectively, in a non-Newtonian xanthan fluid. The viscosity ratio as defined in Eq. (12) takes the same form as the viscosity recovery (Eq. (2)). The time constant,  $\tau$ , was found using transient rheology (Fig. 2) and coefficients  $B, C_1$  and  $C_2$  were determined using the equation limits and a single data point. For  $t \rightarrow \infty$ , the fluid is assumed to be fully recovered and the viscosity experienced by the trailing sphere is equal to the viscosity experienced by the leading sphere, or a single sphere, i.e.  $\mu_2/\mu_1 = \mu_s/\mu_2 = 1$ . Using Eq. (12), where  $t = \infty$  and  $\mu_s/\mu_2 = 1, B = 1$  was deduced.

A single data point ( $V_2/V_s = 1.90, d/r = 29.64, t = 1.67$  s) was used to calculate  $C_1$  and  $C_2$ . This separation ( $d/r \sim 30$ ) was chosen because the fluid disturbance from the leading sphere is small (see fluid velocity in Fig. 7) and therefore the hydrodynamic interactions and fluid viscosity decrease due to shear thinning are expected to be negligible. The values of  $\mu_s/\mu_2 = V_2/V_s = 1.90$  and  $t = 1.67$  s were substituted into Eq. (12). The ratio of  $C_1/C_2$  was assumed to be equal to Eq. (2), resulting in  $C_1 = -0.300$  and  $C_2 = 0.0337$ .

$$V_1 = V_s + \left(\frac{\mu_s}{\mu_2}\right) \left(1 + \frac{r^2}{6} \nabla^2\right) V_{Z(2)} \Big|_{z=z_1} \quad (10)$$

$$V_2 = \left(\frac{\mu_s}{\mu_2}\right) V_s + \left(1 + \frac{r^2}{6} \nabla^2\right) V_{Z(1)} \Big|_{z=z_2} \quad (11)$$

$$\frac{\mu_2}{\mu_s} = B + C_1 e^{-\frac{t}{\tau_1}} + C_2 e^{-\frac{t}{\tau_2}} \quad (12)$$

Fig. 8 shows the sphere velocity ( $V_1/V_s$  and  $V_2/V_s$ ) for two vertically aligned spheres settling along their line of centres in a non-Newtonian xanthan fluid. The symbols show the sphere velocities measured from two-sphere settling experiments (square – leading sphere, circle – trailing sphere). The error bars show 1 standard deviation from the mean

sphere velocity averaged over 1 mm divisions. The sphere velocities calculated from PIV (Eqs. (10)–(12)) are shown by the solid line (leading sphere) and dash line (trailing sphere).

The increased settling velocity of the trailing sphere is clearly shown for both measured and calculated values. At the largest separations of  $d/r \sim 120$ ,  $V_1 \approx V_S$  and  $V_2 \approx 1.35V_S$ . For  $d/r > 30$ , the calculated sphere velocities are within 1 standard deviation of the experimental data, confirming our assumption that the fluid viscosity change due to shear thinning is negligible in this region and therefore acceptable for calculating the values of  $C_1$  and  $C_2$ . At smaller separations ( $d/r < 30$ ), the velocity of the leading sphere increases due to hydrodynamic interactions between the two spheres. This corresponds with the increase in fluid velocity around a single sphere, see Fig. 7, where  $-30 < z/r < 0$ . The range of hydrodynamic interactions is smaller in the non-Newtonian xanthan fluid ( $d/r < 30$ ) than the Newtonian fluid ( $d/r < \sim 40$ , see Fig. 5) and the interaction is weaker even at small separations, in agreement with literature [38,39].

The calculated and measured velocities for the leading sphere are remarkably similar; within 1 standard deviation of the experimental data when  $d/r > 7$ . This suggests that the fluid viscosity decrease, due to shear thinning of the xanthan fluid induced by the settling of a  $r = 0.75$  mm stainless steel sphere, is small even at small sphere-sphere separations. This agrees with a simple calculation of fluid viscosity from the shear rate using the Carreau fit (Eq. (1)). The shear rate,  $\dot{\gamma} = V/2r$  was used as it gives the lowest values of  $\dot{\gamma}$  and equates to the region of highest shear thinning gradient (see Fig. 1). Using an equivalent volume radius for the doublet, the viscosity ( $\mu_{\text{doublet}} = 0.296$  Pa s) is 5.3% lower than the viscosity calculated for a single sphere using the same method ( $\mu_S = 0.313$  Pa s). Our calculations estimate that the fluid viscosity decrease due to thixotropy is 28% for touching spheres, over 5 times larger than the shear thinning contribution. This simple calculation uses the steady state viscosity and neglects the time taken for the new fluid structure to be established. For the faster settling doublet, the time over which the fluid experiences peak stress is shorter and thus the viscosity reduction due to ‘shear thinning’ will be less than the 5.3% viscosity reduction calculated at steady state. We conclude that our assumption of the fluid viscosity decrease due to shear thinning is comparatively smaller than the fluid viscosity decrease due to thixotropy is valid.

When  $d/r < 30$ , the calculated velocity of the trailing sphere shows a minimum due to the sphere interacting with the negative wake of the leading sphere (Fig. 70  $< z/r < 30$ ), however, this is not reflected in the measured data. The inset in Fig. 8 shows a single dataset for  $V_2/V_S$  for  $0 < d/r < 30$  and displays the same increased trailing sphere velocity in the  $10 < d/r < 25$  region, suggesting that this is not an artefact of averaging.

The observed divergence between measured and calculated values occurs in the region of the negative wake. Harlen [13] suggested that the negative wake is formed due to the competition of extensional stresses (which form an extended wake) and relaxation of elastic stresses generated by the shear regions near the sphere surface. At small separations, the extensional stresses are reduced as evidenced by a region of plug flow between the two spheres in yield stress fluids [38,40]. Therefore it is reasonable to assume that viscoelasticity is the largest contributing factor. Previous experiments using Boger fluids (constant viscosity, viscoelastic fluids) produced a decrease in separation between two spheres settling along their line of centres. The convergence of the spheres results from the normal stress difference caused by curved streamlines which envelope both spheres, avoiding the high resistance region between the spheres [20,21].

#### 4. Conclusions

The summative nature of Newtonian flow fields at low  $Re$  was used to validate our experimental procedures and formed the basis for predicting settling spheres in a non-Newtonian xanthan fluid. Faxén’s first law was used to predict the velocities of two  $r = 0.75$  mm spheres set-

ting with vertical alignment in a 95 vol% glycerol + 5 vol% water solution. The fluid velocities calculated from Stokes stream function and experimentally measured (PIV) were used in Faxén’s first law and good agreement was found with the experimental data of two spheres settling in vertical alignment.

For the non-Newtonian xanthan fluid, a viscosity ratio in the form of an exponential decay function was introduced to account for the reduced viscosity experienced by the trailing sphere due to thixotropy. The exponents of the decay function were formed by the time between two spheres normalised by the recovery time constants  $\tau_1$  and  $\tau_2$  obtained from transient rheology measurements. The coefficients were calculated using the limits of  $V_1 = V_2 = V_S$  at large separations and a single data set ( $d/r \approx 30$ ) both of which were found experimentally.

The calculated sphere settling velocities showed good agreement when compared to experimental sphere velocities of two vertically aligned spheres settling in a non-Newtonian xanthan fluid. Our model uses readily obtained experimental parameters to determine the settling velocity of two identical spheres settling with vertical alignment in a non-Newtonian fluid. These parameters are: (i) the single sphere velocity, (ii) a single data point of  $V_2$  and time since  $V_1$  passed, (iii) the fluid rheology and (iv) the fluid velocity caused by a single settling sphere. These values were determined experimentally to reduce the errors currently associated with predictions in non-Newtonian fluids. The method neglects the shear thinning contribution to the viscosity decrease, which we show is small compared to the thixotropic contribution. This is something which should be considered in a fluid with a higher degree of shear thinning or lower thixotropy.

A secondary result of this method is that the overall fluid velocity caused by two vertically aligned spheres settling in a non-Newtonian xanthan fluid can be predicted (for more information see Appendix B). Summing the individual fluid velocity (measured by PIV and scaled by the sphere velocity) for each sphere at each location produces the overall fluid velocity,  $V_F$ . The agreement with the fluid velocity caused by two vertically aligned settling spheres is good. This provides further evidence that the proposed method to describe the settling of spheres in non-Newtonian xanthan fluids is good and there is promise that if the method was extended to two or three dimensions, the fluid velocity field around multiple settling spheres could be captured.

As there are reports [9] that the fluid velocity around a single settling sphere scales with the terminal settling velocity and sphere radius, there is potential for this model to be extended for use with different radius and density spheres using a single fluid velocity profile. This would be particularly useful as in reality most particles are not completely similar.

#### Data statement

Katherine Moseley, Michael Fairweather, David Harbottle (2019): Data associated with ‘Settling dynamics of two identical vertical aligned spheres in a thixotropic fluid.’ University of Leeds. [Dataset]. <https://doi.org/10.5518/708>, Article metadata is available under a Creative Commons Attribution licence (CC-BY).

#### Acknowledgements

The research was completed at the University of Leeds as part of the Engineering and Physical Sciences Research Council (EPSRC) Centre for Doctoral Training in Next Generation Nuclear (EP/L015390/1), which forms part of the doctoral studies of K.M..

#### Appendix A. Oscillatory shear rheology

The response of the non-Newtonian fluid (0.25 wt% xanthan, 59.85 wt% glycerol, 39.9 wt% water) under small amplitude oscillatory shear (SAOS) was first studied using a strain amplitude ( $\gamma_0$ ) sweep between 0.01 and 10 at 1 rad/s to determine the limit of the linear viscoelastic response ( $\gamma_0 \sim 0.25$ ). A frequency sweep ( $0.05 < \omega < 100$  rad/s)

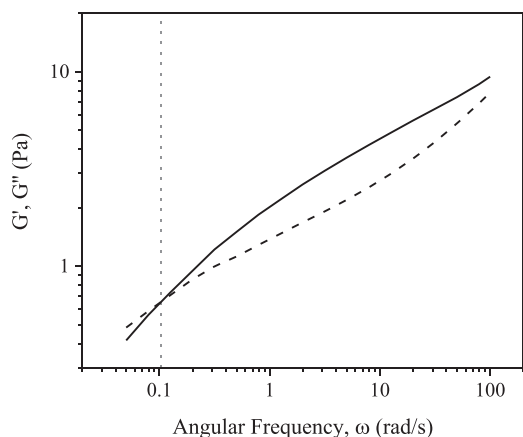


**Fig. A1.** Frequency sweep at a strain of 0.15 of a representative solution (0.25 wt% xanthan, 59.85 wt% glycerol, 39.9 wt% water). Solid and dash lines represent the storage ( $G'$ ) and loss ( $G''$ ) moduli respectively. Vertical dot line indicates the cross over frequency,  $\omega_c = 0.104$  rad/s.

was then conducted at  $\gamma_0 = 0.15$  and is shown in Fig. A1. The solid and dash lines represent the storage ( $G'$ ) and loss ( $G''$ ) moduli respectively. The reciprocal of the cross over frequency ( $\omega_c = 0.104$  rad/s indicated by the dot line in Fig. A1) where  $G' = G''$  is considered a characteristic elastic timescale [28].

The small deformations in SAOS may not be representative as the structure is not destroyed [29] so further measurements were taken at larger amplitudes. Large amplitude oscillatory shear (LAOS) measurements were taken at angular frequencies ( $\omega$ ) of {0.1, 1} (rad/s) and strains ( $\gamma_0$ ) of {0.178, 0.316, 0.562, 1, 1.78, 3.16} (–) and analysed

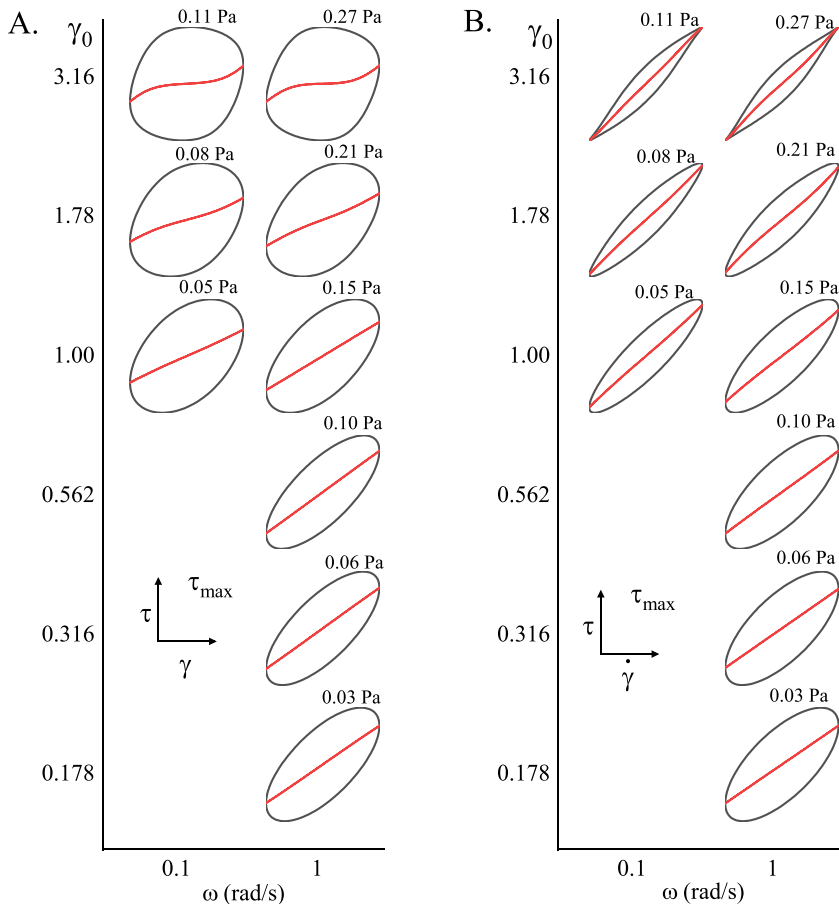


**Fig. A2.** Lissajous curves of stress against strain (A) and strain rate (B) positioned in Pipkin space according to input variables strain ( $\gamma_0$ ) and angular frequency ( $\omega$ ) for a representative solution (0.25 wt% xanthan, 59.85 wt% glycerol, 39.9 wt% water). Red lines show decomposed elastic (A) and viscous (B) stresses. Max stress ( $\tau_{max}$ ) is indicated for each curve. (For interpretation of the references to color in this figure legend, the reader is referred to the web version of this article.)

using the MITlaos software [41]. Fig. A2 shows the Lissajous curves of stress against strain (A) and strain rate (B). Red lines show decomposed elastic (A) and viscous (B) stress. Low frequency and strain amplitude data is not included due to low signal to noise ratios. Low strain amplitude ( $\gamma_0 = 0.178$ ) show linear responses and strain amplitude sweeps show that the linear regime remains up to  $\gamma_0 \sim 0.25$ . Decreasing  $G'$  and  $G''$  in strain amplitude sweeps suggests inter-cycle strain softening and shear thinning behaviour [41,42]. Fig. A2(A) shows intra-cycle strain stiffening (convexity of elastic stresses) and Fig. A2(B) shows weak shear thinning (concavity of viscous stresses) at the largest strain amplitudes ( $\gamma_0 = 1.78$  and 3.16). The dominant behaviour is strain softening. Strain stiffening observed in the Lissajous curves is a local effect which can also be interpreted as strain rate dominated softening [42,43]. Non-linearities increase with increasing amplitude but remain relatively small in this range of strains (the intensity of the third harmonic of the Fourier transform normalised by the intensity of the 1st harmonic,  $I_3/I_1 < 10\%$ ).

The area enclosed by the stress-strain curve is related to the energy dissipated over the cycle (viscous contribution). Fig. A2 shows a clear increase in enclosed area, suggesting the viscous contribution dominates at large strain amplitudes. Decreasing elasticity with increasing strain amplitude, and weak dependence on angular frequency (increasing elasticity with increasing frequency) agrees with other LAOS measurements of xanthan solutions [29,44].

**Appendix B. Overall fluid velocity**

The overall fluid velocity ( $V_F$ ) caused by two vertically aligned spheres settling in a shear thinning fluid can be predicted by summing the individual fluid velocity caused by each sphere at each location. Eqs. (10) and (11) can be separated into 2 terms; the first term is the

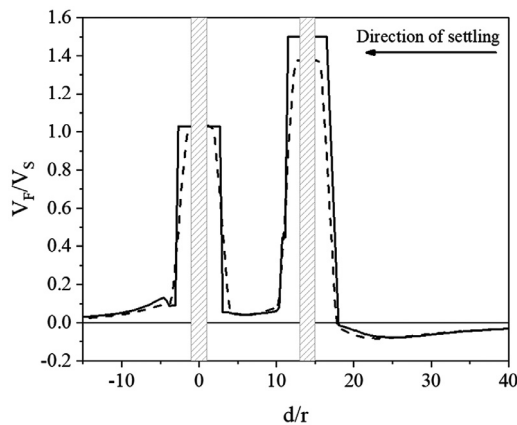


**Fig. A3.** Fluid velocity around two vertically aligned spheres settling in a non-Newtonian xanthan fluid. The leading sphere is centred at  $d/r=0$  and the trailing sphere is centred at  $d/r=14.0$  (shaded regions). The solid line shows the measured fluid velocity (PIV) and the dash line shows the calculated fluid velocity (Eq. (A1)).

velocity contribution of the sphere of interest, and the second term is the fluid velocity contribution of the other sphere. If the fluid velocity, which are the second terms of Eqs. (10) and (11), are summed at all values of  $z$ , the overall fluid velocity,  $V_F$  can be calculated. The first term in Eq. (A1) is the fluid velocity contribution of the leading sphere  $V_{Z(1)}$ . The second term is the trailing sphere fluid velocity  $V_{Z(2)}$ , adjusted for the lower viscosity using the viscosity ratio (Eq. (12)) and sphere position ( $z = z - d$ ).

$$V_F = \left(1 + \frac{r^2}{6} \nabla^2\right) V_{Z(1)} + \left(\frac{\mu_S}{\mu_2}\right) \left(1 + \frac{r^2}{6} \nabla^2\right) V_{Z-d(2)} \quad (\text{A1})$$

Fig. A3 shows the calculated fluid velocity around 2 spheres  $d/r=14.0$  shown in Fig. A3 is in the region of the negative wake. In Fig. 8 we showed that the calculated sphere velocity is underpredicted in this region when compared to the experimental data. Unfortunately, due to the field of view of the PIV camera and desire to show the fluid velocity ahead of and behind the spheres, a larger separation (where the sphere velocity agreement is better) cannot be shown.

As expected, the calculated trailing sphere velocity is lower than the measured velocity (by 7.5%). The calculated leading sphere velocity is in good agreement with the measured velocity (overestimated by 0.17%). The measured and calculated fluid velocities appear to be in good agreement, despite the discrepancy in trailing sphere velocity. The difference between the measured and calculated velocities is less than  $0.03 \times V_S$  but the small fluid velocity relative to the sphere velocity should be noted. Due to the changing separation, the error associated with the measured velocity could not be quantified.

## References

- [1] S. Bobroff, R.J. Phillips, Nuclear magnetic resonance imaging investigation of sedimentation of concentrated suspensions in non-Newtonian fluids, *J. Rheol.* (N. Y. N. Y.) 42 (6) (1998) 1419–1436, doi:10.1122/1.550895.
- [2] E. Allen, P.H.T. Uhlherr, Nonhomogeneous sedimentation in viscoelastic fluids, *J. Rheol.* (N. Y. N. Y.) 33 (4) (1989) 627–638, doi:10.1122/1.550030.
- [3] S. Daugan, L. Talini, B. Herzhaft, C. Allain, Aggregation of particles settling in shear-thinning fluids, *Eur. Phys. J. E* 7 (1) (2002) 73–81, doi:10.1140/epje/i200101116.
- [4] D.D. Joseph, Y.J. Liu, M. Poletto, J. Feng, Aggregation and dispersion of spheres falling in viscoelastic liquids, *J. Nonnewton. Fluid Mech.* 54 (1994) 45–86, doi:10.1016/0377-0257(94)80015-4.
- [5] M.M. Gumulya, R.R. Horsley, K.C. Wilson, The settling of consecutive spheres in viscoplastic fluids, *Int. J. Miner. Process* 82 (2) (2007) 106–115, doi:10.1016/j.minpro.2006.11.005.
- [6] E. Verneuil, R.J. Phillips, L. Talini, Axisymmetric two-sphere sedimentation in a shear thinning viscoelastic fluid: particle interactions and induced fluid velocity fields, *J. Rheol.* (N. Y. N. Y.) 51 (6) (2007) 1343–1359, doi:10.1122/1.2780799.

- [7] D. Sighi, M. Coutanceau, Effect of finite boundaries on the slow laminar isothermal flow of a viscoelastic fluid around a spherical obstacle, *J. Nonnewton. Fluid Mech.* 2 (1) (1977) 1–21, doi:10.1016/0377-0257(77)80029-3.
- [8] G. Gheissary, B.H.A.A. Van Den Brule, Unexpected phenomena observed in particle settling in non-Newtonian media, *J. Nonnewton. Fluid Mech.* 67 (1996) 1–18, doi:10.1016/S0377-0257(96)01436-X.
- [9] M.T. Arigo, G.H. McKinley, An experimental investigation of negative wakes behind spheres settling in a shear-thinning viscoelastic fluid, *Rheol. Acta* 37 (4) (1998) 307–327, doi:10.1007/s003970050118.
- [10] R.P. Chhabra, *Bubbles, Drops, and Particles in Non-Newtonian Fluids*, CRC press, 2006.
- [11] C. Bisgaard, Velocity fields around spheres and bubbles investigated by laser-doppler anemometry, *J. Nonnewton. Fluid Mech.* 12 (3) (1983) 283–302, doi:10.1016/0377-0257(83)85003-4.
- [12] M.R. Horsley, R.R. Horsley, K.C. Wilson, R.L. Jones, Non-Newtonian effects on fall velocities of pairs of vertically aligned spheres, *J. Nonnewton. Fluid Mech.* 124 (1–3) (2004) 147–152, doi:10.1016/j.jnnfm.2004.09.002.
- [13] O.G. Harlen, The negative wake behind a sphere sedimenting through a viscoelastic fluid, *J. Nonnewton. Fluid Mech.* 108 (1–3) (2002) 411–430, doi:10.1016/S0377-0257(02)00139-8.
- [14] D.A. Eisenberg, I.M. Klink, R.J. Phillips, Axisymmetric sedimentation of spherical particles in a viscoelastic fluid: sphere–wall and sphere–sphere interactions, *J. Rheol.* (N. Y. N. Y.) 57 (3) (2013) 857–880, doi:10.1122/1.4798625.
- [15] M.B. Bush, On the stagnation flow behind a sphere in a shear-thinning viscoelastic liquid, *J. Nonnewton. Fluid Mech.* 55 (3) (1994) 229–247, doi:10.1016/0377-0257(94)80072-3.
- [16] J.V. Satrape, M.J. Crochet, Numerical simulation of the motion of a sphere in a booger fluid, *J. Nonnewton. Fluid Mech.* 55 (1) (1994) 91–111, doi:10.1016/0377-0257(94)80061-8.
- [17] H.S. Dou, N. Phan-Thien, Negative wake in the uniform flow past a cylinder, *Rheol. Acta* 42 (5) (2003) 383–409, doi:10.1007/s00397-003-0293-z.
- [18] E.T.G. Bot, M.A. Hulsen, B.H.A.A. Van Den Brule, The motion of two spheres falling along their line of centres in a Boger fluid, *J. Nonnewton. Fluid Mech* 79 (2–3) (1998) 191–212, doi:10.1016/S0377-0257(98)00106-2.
- [19] M.J. Riddle, C. Narvaez, R.B. Bird, Interactions between two spheres falling along their line of centers in a viscoelastic fluid, *J. Nonnewton. Fluid Mech.* 2 (1) (1977) 23–35, doi:10.1016/0377-0257(77)80030-X.
- [20] R.J. Phillips, L. Talini, Chaining of weakly interacting particles suspended in viscoelastic fluids, *J. Nonnewton. Fluid Mech.* 147 (3) (2007) 175–188, doi:10.1016/j.jnnfm.2007.08.007.
- [21] R.J. Phillips, Dynamic simulation of hydrodynamically interacting spheres in a quiescent second-order fluid, *J. Fluid Mech* 315 (1996) 345–365, doi:10.1017/S0022112096002455.
- [22] M. Hariharaputhiran, R.S. Subramanian, G.A. Campbell, R.P. Chhabra, The settling of spheres in a viscoplastic fluid, *J. Nonnewton. Fluid Mech* 79 (1) (1998) 87–97, doi:10.1016/S0377-0257(98)00084-6.
- [23] Z. Yu, A. Wachs, Y. Peysson, Numerical simulation of particle sedimentation in shear-thinning fluids with a fictitious domain method, *J. Nonnewton. Fluid Mech.* 136 (2–3) (2006) 126–139, doi:10.1016/j.jnnfm.2006.03.015.
- [24] M.M. Gumulya, R.R. Horsley, K.C. Wilson, V. Pareek, A new fluid model for particles settling in a viscoplastic fluid, *Chem. Eng. Sci.* 66 (4) (2011) 729–739, doi:10.1016/j.ces.2010.11.037.
- [25] J. Happel, R. Pfeffer, The motion of two spheres following each other in a viscous fluid, *AIChE J* 6 (1) (1960) 129–133, doi:10.1002/aic.690060125.
- [26] P.J. Carreau, Rheological equations from molecular network theories, *Trans. Soc. Rheol* 16 (1) (1972) 99–127, doi:10.1122/1.549276.
- [27] J. Mewis, N.J. Wagner, Thixotropy, *Adv. Colloid Interface Sci* 147–148 (2009) 214–227, doi:10.1016/j.cis.2008.09.005.
- [28] T.G. Mezger, *The Rheology Handbook, for Users of Rotational and Oscillatory Rheometers*, 2014 doi:Artn 073303.r/doi 10.1063/1.2966151.
- [29] K. Hyun, M. Wilhelm, C.O. Klein, K.S. Cho, J.G. Nam, K.H. Ahn, S.J. Lee, R.H. Ewoldt, G.H. McKinley, A review of nonlinear oscillatory shear tests: analysis and application of large amplitude oscillatory shear (LAOS), *Prog. Polym. Sci.* 36 (12) (2011) 1697–1753, doi:10.1016/j.progpolymsci.2011.02.002.
- [30] J. Happel, H. Brenner, in: *Low Reynolds Number Hydrodynamics*, 40, Englewood Cliffs NJ, 1983, pp. 25–45, doi:10.1146/annurev.fluid.39.050905.110231.
- [31] T. Bohlin, *On the Drag on A Rigid Sphere Moving in A Viscous Liquid Inside a Cylindrical Tube*, Elander, 1960.
- [32] H. Lamb, *Hydrodynamics*, Cambridge University Press, Cambridge, 1895.
- [33] M. Stimson, G.B. Jeffery, The motion of two spheres in a viscous fluid, *Proc. R. Soc. A Math. Phys. Eng. Sci.* 111 (757) (1926) 110–116, doi:10.1098/rspa.1926.0053.
- [34] H. Faxén, Der Widerstand gegen die Bewegung einer starren Kugel in einer zähen Flüssigkeit, die zwischen zwei parallelen ebenen Wänden eingeschlossen ist, *Ann. Phys* 373 (10) (1922) 89–119, doi:10.1002/andp.19223731003.
- [35] S. Kim, S.J. Karrila, *Microhydrodynamics: Principles and Selected Applications*, Butterworth-Heinemann, 1991.
- [36] A.M.V. Putz, T.I. Burghelca, I.A. Frigaard, D.M. Martinez, Settling of an isolated spherical particle in a yield stress shear thinning fluid, *Phys. Fluids* 20 (3) (2008) 033102, doi:10.1063/1.2883937.
- [37] B. Gueslin, L. Talini, B. Herzhaft, Y. Peysson, C. Allain, Flow induced by a sphere settling in an aging yield-stress fluid, *Phys. Fluids* 18 (10) (2006) 103101, doi:10.1063/1.2358090.
- [38] B.T. Liu, S.J. Muller, M.M. Denn, Interactions of two rigid spheres translating collinearly in creeping flow in a Bingham material, *J. Nonnewton. Fluid Mech* 113 (1) (2003) 49–67, doi:10.1016/S0377-0257(03)00111-3.

- [39] C. Zhu, K. Lam, H.H. Chu, X.D. Tang, G. Liu, Drag forces of interacting spheres in power-law fluids, *Mech. Res. Commun* 30 (6) (2003) 651–662, doi:[10.1016/S0093-6413\(03\)00067-3](https://doi.org/10.1016/S0093-6413(03)00067-3).
- [40] P. Jie, K.Q. Zhu, Drag force of interacting coaxial spheres in viscoplastic fluids, *J. Nonnewton. Fluid Mech* 135 (2–3) (2006) 83–91, doi:[10.1016/j.jnnfm.2006.01.006](https://doi.org/10.1016/j.jnnfm.2006.01.006).
- [41] R.H. Ewoldt, A.E. Hosoi, G.H. McKinley, New measures for characterizing nonlinear viscoelasticity in large amplitude oscillatory shear, *J. Rheol. (N. Y. N. Y)* 52 (6) (2008) 1427–1458, doi:[10.1122/1.2970095](https://doi.org/10.1122/1.2970095).
- [42] M.R.B. Mermet-Guyennet, J. Gianfelice de Castro, M. Habibi, N. Martzel, M.M. Denn, D. Bonn, LAOS: the strain softening/strain hardening paradox, *J. Rheol. (N. Y. N. Y)* 59 (1) (2014) 21–32, doi:[10.1122/1.4902000](https://doi.org/10.1122/1.4902000).
- [43] R.H. Ewoldt, N.A. Bharadwaj, Low-dimensional intrinsic material functions for nonlinear viscoelasticity, *Rheol. Acta* 52 (3) (2013) 201–219, doi:[10.1007/s00397-013-0686-6](https://doi.org/10.1007/s00397-013-0686-6).
- [44] R.H. Ewoldt, P. Winter, J. Maxey, G.H. McKinley, Large amplitude oscillatory shear of pseudoplastic and elastoviscoplastic materials, *Rheol. Acta* 49 (2) (2010) 191–212, doi:[10.1007/s00397-009-0403-7](https://doi.org/10.1007/s00397-009-0403-7).